RSC Advances

PAPER

View Article Online
View Journal | View Issue

Cite this: *RSC Adv.*, 2024, **14**, 771

Component-controlled synthesis of Pd_xSn_y nanocrystals on carbon nanotubes as advanced electrocatalysts for oxygen reduction reaction†

Weibin Guo,[a] Rui Yang,[bc] Jiayao Fan,[b] Xing Xiang,[a] Xuehui Du,[a] Naien Shi,*[ac] Jianchun Bao [b] and Min Han *[ab]

Received 9th November 2023
Accepted 17th December 2023

DOI: 10.1039/d3ra07657a

rsc.li/rsc-advances

Pd-based bimetallic or multimetallic nanocrystals are considered to be potential electrocatalysts for cathodic oxygen reduction reaction (ORR) in fuel cells. Although much advance has been made, the synthesis of component-controlled Pd–Sn alloy nanocrystals or corresponding nanohybrids is still challenging, and the electrocatalytic ORR properties are not fully explored. Herein, component-controlled synthesis of Pd_xSn_y nanocrystals (including Pd_3Sn, Pd_2Sn, Pd_3Sn_2, and PdSn) has been realized, which are *in situ* grown or deposited on pre-treated multi-walled carbon nanotubes (CNTs) to form well-coupled nanohybrids (NHs) by a facile one-pot non-hydrolytic system thermolysis method. In alkaline media, all the resultant Pd_xSn_y/CNTs NHs are effective at catalyzing ORR. Among them, the Pd_3Sn/CNTs NHs exhibit the best catalytic activity with the half-wave potential of 0.85 V (*vs.* RHE), good cyclic stability, and excellent methanol-tolerant capability due to the suited Pd–Sn alloy component and its strong interaction or efficient electronic coupling with CNTs. This work is conducive to the advancement of Pd-based nanoalloy catalysts by combining component engineering and a hybridization strategy and promoting their application in clean energy devices.

1. Introduction

Efficient electrochemical energy conversion and storage devices play a critical role in mitigating global climate change and energy crises.[1–5] Recently, electrochemical energy conversion and storage devices using oxygen as raw materials, such as fuel cells and metal–oxygen batteries, have been widely studied owing to their high theoretical energy density and environmental friendliness, but the development of such devices is still limited by the slow oxygen reduction reaction (ORR) kinetics.[6–10] Pt-based catalysts are currently the dominant type of catalysts for oxygen reduction, but they suffer from low abundance, high cost, and poor resistance to CO molecules, which limit their commercial applications.[11–15] Consequently, exploring alternative non-Pt-based catalysts with enhanced ORR activity and stability has attracted extensive attention in recent years.

To date, many low-cost non-Pt-based catalysts have been explored, such as metal oxides,[16,17] heteroatom-doped carbon materials,[18–20] and metal–organic skeleton materials,[21–23] but these catalysts are far from meeting the requirements of high activity and stability of ORR.[4,13] Several approaches have been proposed to improve the ORR activity and stability of non-Pt-based catalysts, including regulating the electronic configuration, oxygen adsorption strength, and stability through compositional control and selecting appropriate catalyst supports.[24–28] As for the composition regulation, Pd-based catalysts, particularly Pd-based bimetallic catalysts, have been intensively investigated due to Pd's similar electronic configuration to Pt, higher abundance, and lower cost compared with Pt.[29–31] The design concept of Pd-based bimetallic catalysts is to improve ORR activity while reducing the cost of catalyst by introducing cheap secondary metals such as Cu,[32,33] Zn,[34] Ni,[35] Co,[36,37] Fe,[38] Mn,[39] Mo,[29] and Sn.[40] Among them, Sn is abundant, cheap, and can form a variety of nanocrystalline alloys with palladium.[41–43] The preparation of Pd–Sn bimetallic nanostructures is of great significance for improving the ORR activity and stability of Pd-based catalysts.[44,45] In terms of the selection of catalyst support materials, carbon-based materials such as graphene, carbon blacks, nitrogen-doped carbon materials, and carbon nanotubes (CNTs) are widely used due to their high electrical conductivity, specific surface area, and affordability.[24,46] Among them, CNTs are ideal catalyst support materials due to their strong flexibility and hollow tubular structure, which is conducive to accelerating electron transfer and mass transfer

[a]*Fujian Cross Strait Institute of Flexible Electronics (Future Technologies), Fujian Normal University, Fuzhou 350117, P. R. China. E-mail: ifeneshi@fjnu.edu.cn*

[b]*Jiangsu Key Laboratory of New Power Batteries, Jiangsu Key Laboratory of Biofunctional Materials, School of Chemistry and Materials Science, Nanjing Normal University, Nanjing 210023, P. R. China. E-mail: 07203@njnu.edu.cn*

[c]*Key Laboratory for Organic Electronics and Information Displays, Institute of Advanced Materials, Nanjing University of Posts & Telecommunications, Nanjing 210023, P. R. China*

† Electronic supplementary information (ESI) available. See DOI: https://doi.org/10.1039/d3ra07657a

process.[46] Despite these efforts, it remains a challenge to further improve ORR performance by integrating active Pd–Sn bimetallic nanostructures onto CNTs through a simple synthetic pathway.

In this work, we report the controllable synthesis and characterization of a series of Pd_xSn_y (including Pd_3Sn, Pd_2Sn, Pd_3Sn_2, and PdSn) intermetallic NCs that coupled with multi-walled CNTs nanohybrids (NHs), which were synthesized by a facile one-pot non-hydrolytic system thermolysis method. By only adjusting the molar ratios of Pd and Sn precursors, the Pd_3Sn/CNTs, Pd_2Sn/CNTs, Pd_3Sn_2/CNTs, and PdSn/CNTs NHs are easily obtained. The synthetic protocol is simple, environmentally friendly, reproducible, and easy for mass production. Electrocatalytic tests reveal that Pd_xSn_y/CNTs NHs are capable of catalyzing ORR in alkaline conditions. Among them, the Pd_3Sn/CNTs NHs display the best catalytic activity with an onset potential of 1.02 V (*vs.* RHE) and a half-wave potential of 0.85 V (*vs.* RHE), surpassing most of recently reported Pd-based bimetallic or multimetallic alloys catalysts. Moreover, the Pd_3Sn/CNTs NHs manifest good durability and are capable of continuously operating for 5000 cycles without a significant decrease in catalytic activity. Furthermore, the methanol-tolerant capability of such Pd_3Sn/CNTs NHs outperforms Pt/C catalysts. This work presents a novel and promising way to prepare Pd_xSn_y/CNTs NHs, which have significant practical value in the field of energy technology.

2. Experimental section

2.1 Pre-treatment of carbon nanotubes

The CNTs (1.25 g) were firstly refluxed in 92.5 mL of 6 M nitric acid aqueous solution and vigorously stirred in an oil bath at 80 °C for 24 h. Upon cooling naturally, centrifugation was used to separate the surface-functionalized CNTs, and washing with deionized water repeatedly until the supernatant solution was neutral. After that, the obtained black product was dried overnight under a vacuum at 50 °C and used for subsequent experiments.

2.2 Synthesis of Pd_xSn_y/CNTs NHs

The Pd_xSn_y/CNTs NHs were synthesized *via* a facile one-pot non-hydrolytic system thermolysis method by regulating the used Pd and Sn metal precursors' molar ratios. The typical Pd_3Sn/CNTs NHs were prepared as follows: 1.5 mmol of $C_4H_6O_4Pd$ and 876 mg of pre-treated CNTs (20 wt%) were mixed into 10 mL of octadecene and 10 mL of oleylamine in a clean 250 mL three-necked round flask, and then stirred and ultrasonically treated for 10 min to form a homogenous solution. After that, 0.5 mmol of $C_{16}H_{36}Sn$ was added to the above solution and continuously stirred for 5 min. Subsequently, the reactor was transferred into the sand bath, and heated to 240 °C for 0.5 h. Upon cooling naturally, centrifugation was used to separate the crude product, and the by-products were cleared by washing with *n*-heptane and anhydrous ethanol. The obtained black product was dried overnight under a vacuum at 50 °C and used for subsequent analysis.

The synthesis of Pd_2Sn/CNTs, Pd_3Sn_2/CNTs, and PdSn/CNTs NHs were similar to that for Pd_3Sn/CNTs, and the only difference was that by turning the Pd and Sn metal precursors' molar ratios to 2 : 1, 3 : 2 and 1 : 1, respectively.

2.3 Materials characterization

The X-ray diffraction patterns were collected by Rigaku's X-ray diffractometer. The transmission electron microscopy (TEM), high-resolution TEM (HRTEM), and energy dispersive spectrometer (EDS) images were characterized by JEOL-2100F and JEM ARM 200F. The Raman spectra were measured by a Raman spectrum (JY HR 800). The surface chemical states of samples were analyzed by the X-ray photoelectron spectra (XPS, ESCALAB Xi^+).

2.4 Electrocatalytic measurements

The electrocatalytic tests were executed on a Rotating Electrode (Gamry) with a glassy carbon disk. All electrochemical tests were performed at room temperature on a three-electrode system utilizing an electrochemical workstation (CHI700E), in which the Pd_xSn_y/CNTs NHs ink-modified glassy carbon disk electrodes (GCEs), the Ag/AgCl electrode, and Pt sheet were utilized as the working, reference, and counter electrodes, respectively.

The working electrode was prepared as follows: 2.5 mg Pd_3Sn/CNTs NHs was added to 0.5 mL anhydrous ethanol, 0.5 mL deionized water, and 40 μL Nafion solution (5%), and ultrasonic dispersion was made into a uniform catalyst ink. After that, 16 μL of catalyst ink was dropped on the GC rotating ring-disk electrode (RRDE) and dried. The cyclic voltammetry (CV) curves were performed at a scanning rate of 100 mV s^{-1} in N_2- and O_2-saturated 0.1 M KOH electrolyte in the range of −0.8 V to 0.2 V (*vs.* Ag/AgCl). Linear sweep voltammetry (LSV) curves were collected in O_2-saturated 0.1 M KOH electrolyte at a scanning rate of 5 mV s^{-1} in the range of −0.8 V to 0.2 V (*vs.* Ag/AgCl) at speed of 400, 800, 1200, 1600, and 2500 rpm. For comparison, the commercial Pt/C (20%, Alfa Asear) catalyst modified RRDE was also prepared. In this work, all potentials are converted into relatively reversible hydrogen electrode (RHE) values, and the current density is normalized about the geometric area of the glassy carbon.

3. Results and discussion

3.1 Characterization of Pd_xSn_y/CNTs NHs

The schematic diagram of the synthesis of Pd_xSn_y/CNTs NHs is presented in Fig. 1. To effectively capture Pd and Sn precursors on CNTs to grow Pd_xSn_y NCs, the CNTs were firstly treated with concentrated nitric acid to introduce oxygen-containing groups. The overall morphology of CNTs (Fig. S1A and B†) was maintained well after acid treatment. The related Raman spectra (Fig. S1C†) proved that the pre-treated CNTs have a large number of ordered (G band) and disordered (D band) structures.[21,47] Further FT-IR spectra (Fig. S1D†) analyses confirmed that the oxygen-containing

groups had been successfully introduced on the surface of pretreated CNTs, which could provide strong bonding and efficient "landing" sites for the growth of Pd_xSn_y NCs. In a typical synthesis, the proper amount of pre-treated or surface functionalized CNTs was added to the mixed solution containing oleamine and octadecene in a clean 250 mL three-necked round flask, and then the palladium acetate and tetrabutyltin with different molar ratio were added in turn. Subsequently, the reactor was heated to 240 °C for 0.5 h, the desired Pd_xSn_y NCs would nucleate and *in situ* grow or deposit on the surface of CNTs to generate well-coupled NHs.

The component, phase structure, and crystallinity of the typical Pd_3Sn/CNTs NHs were first identified by powder X-ray diffraction (XRD), energy dispersive spectroscopy (EDS), and Raman spectra. Fig. 2A shows the related XRD pattern. The diffraction peaks at 39.3°, 45.5°, 66.7°, and 80.1° belong to the (111), (200), (220), and (311) planes of the cubic phase Pd_3Sn (JCPDS-65-8225), respectively. Except for those four diffraction peaks, another shoulder peak appeared at about 26° belongs to the characteristic (002) planes of CNTs. Further EDS analyses (Fig. S2†) reveal that only Pd, Sn, C, and O elements can be detected in the typical Pd_3Sn/CNTs NHs. The molar ratio of Pd to Sn was estimated to be approximately 3 : 1 based on integration calculation. As for the observed small O peak, it is most likely derived from CNTs' unbound oxygen-containing groups or air. To confirm the existence of the CNTs component, the Raman spectra test was also performed. Two characteristic Raman peaks can be observed at around 1360 and 1582 cm^{-1} (Fig. 2B), corresponding to the D band (disordered C, sp^3 hybridization) and G band (ordered C, sp^2 hybridization) of carbon-based nanostructures, respectively. The above results demonstrate the successful synthesis of Pd_3Sn/CNTs NHs.

To further verify the surface component and chemical states of the Pd_3Sn/CNTs NHs, X-ray photoelectron spectroscopy (XPS) tests were performed. The survey XPS spectra of Pd_3Sn/CNTs NHs (Fig. S3†) further indicate the presence of Pd, Sn, C, and O elements, which is consistent with the XRD and EDS results. Fig. 2C shows the C 1s XPS fine spectra, the signals are deconvoluted into a strong peak centered at 284.8 eV and two weak peaks located at 285.7 and 288.6 eV, which are assigned to C=C, C–O, and O=C–O bonds, respectively.[48] The presence of C–O and O=C–O bonds also affirms the surface group functionalization on CNTs, which is further evidenced by O 1s spectra. Fig. 2D displays that the deconvoluted peaks at 531.1, 531.9, 532.9, and 534.1 eV are corresponding to the binding energies of M–O, O–H, C–O/H_2O and C=O/M–O–C bonds, respectively.[49] The presence of M–O indicates that partial surface metal atoms are oxidized. The Sn 3d spectra (Fig. 2E) present two doublet peaks at 485.6 and 494.0 eV ($3d_{5/2}$ and $3d_{3/2}$ of Sn^0) and 487.0 and 495.5 eV ($3d_{5/2}$ and $3d_{3/2}$ of $Sn^{2+/4+}$), respectively. Notably, the existence of high-valenced Sn is likely owing to the slight surface oxidation of Sn into amorphous SnO_x, as it has a higher affinity for oxygen compared to Pd. Additionally, electron transfer from Sn to Pd on the surface occurs due to the lower electronegativity of Sn relative to Pd. As displayed in the Pd 3d spectrum (Fig. 2F), the binding energies of 336.0, 337.3, and 338.3 eV are attributed to $3d_{5/2}$ peaks for elements Pd^0, Pd^{2+}, and Pd^{4+} respectively.[40,50] Similarly, surface high-valenced Pd can be found in Pd_3Sn/CNTs NHs, but the catalyst is still dominated by metallic Pd. Meanwhile, the addition of Sn is conducive to inhibiting the oxidation of Pd to a certain extent (Fig. S4A–D†), but excessive Sn will reduce the percentage of Pd^0, thus affecting ORR activity.

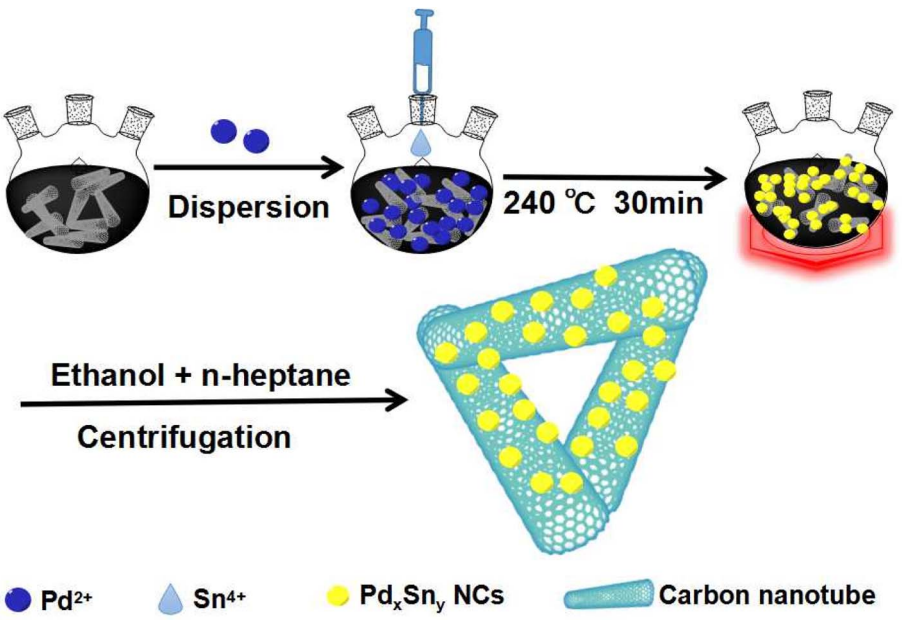

Fig. 1 Diagram of the synthesis process of Pd_xSn_y/CNTs NHs.

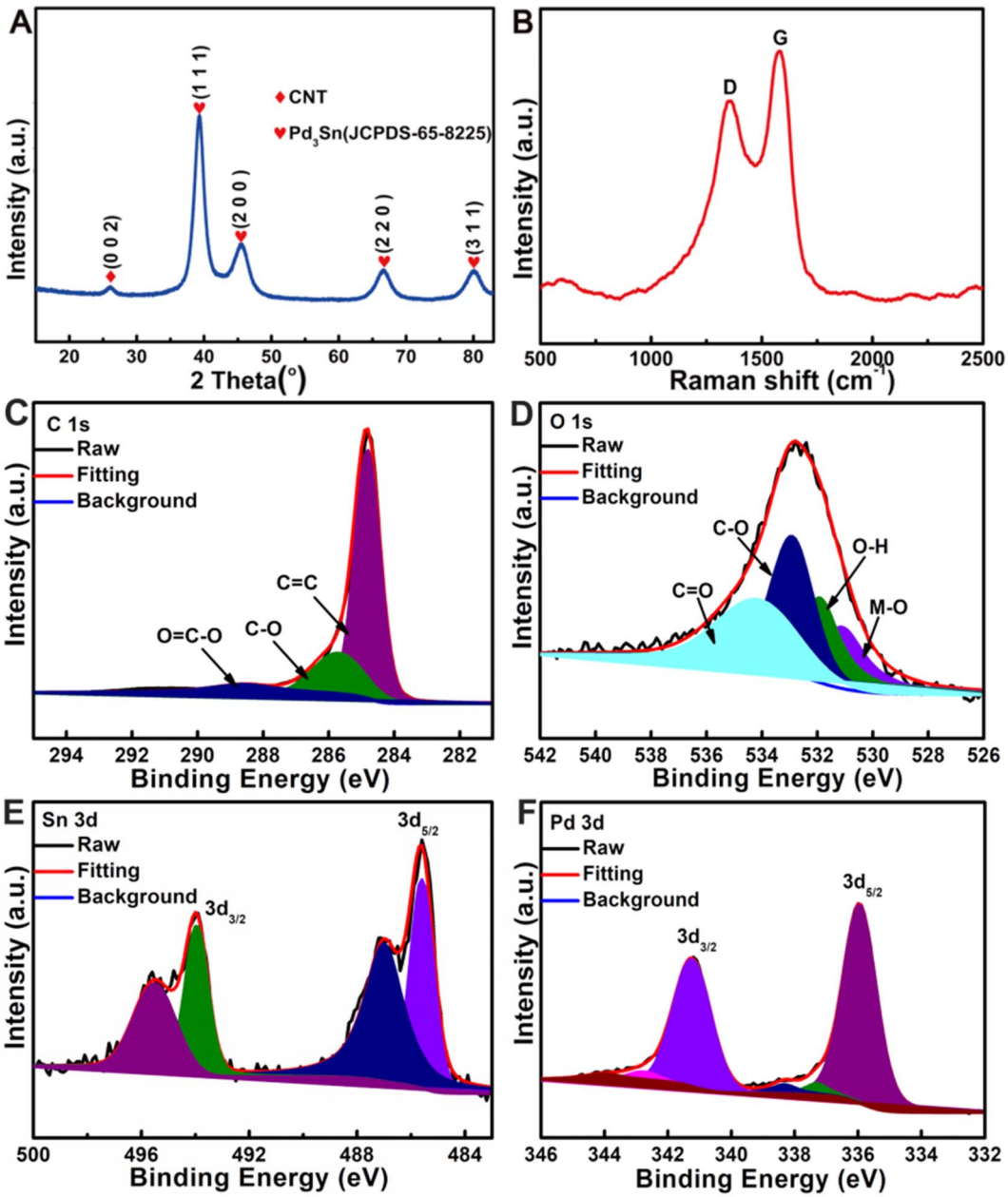

Fig. 2 (A and B) XRD pattern (A) and Raman spectra (B) of Pd_3Sn/CNT NHs. (C–F) The C 1s (C), O 1s (D), Sn 3d (E), and Pd 3d (F) fine XPS spectra for the typical Pd_3Sn/CNT NHs.

The low-magnification transmission electron microscopy (TEM) image (Fig. 3A) displays numerous homogeneous spherical black spots on the gray tubular nanostructures. Based on their contrast variations, it is plausible to infer that the small black spots correspond to the Pd_3Sn NCs, while the gray tubular substances are associated with the CNTs. By conducting a statistical analysis on more than 50 particles, it was determined that the average size of Pd_3Sn NCs is approximately 7.2 nm (inset of Fig. 3A). The high-magnification TEM image (Fig. 3B) of an individual Pd_3Sn/CNTs reveals the spontaneous assembly of small Pd_3Sn NCs into a network-like structure surrounding the outer surface of CNTs. This arrangement promotes electron conduction and electrolyte infiltration. The corresponding high-resolution TEM (HRTEM) image (Fig. 3C) demonstrates a distinct interface between the Pd_3Sn NCs and CNTs with the Pd_3Sn NCs firmly bound to the outer wall of the CNTs. This binding enhances the interaction between the Pd_3Sn NCs and CNTs, thereby improving the stability of the NHs. Moreover, the presence of lattice fringes with a spacing of approximately 0.23 nm, attributed to the (111) plane of the cubic phase Pd_3Sn (JCPDS-65-8225), indicates the existence of Pd_3Sn in the NHs. Additionally, another set of lattice fringes with a spacing of around 0.34 nm, corresponding to the (002) plane

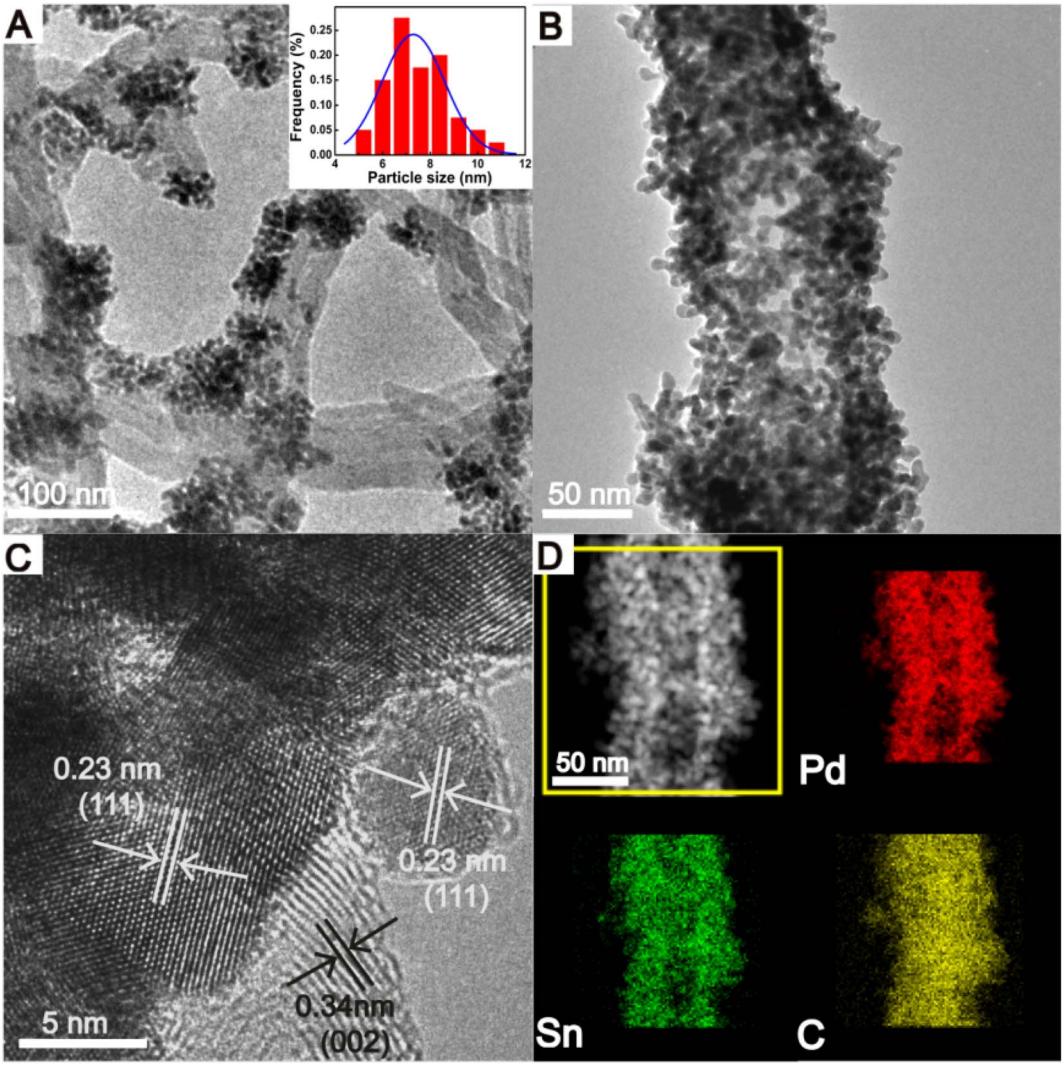

Fig. 3 (A and B) The low- (A) and high- (B) magnification TEM images of the typical Pd_3Sn/CNTs NHs. (C) HRTEM image for the Pd_3Sn NCs on an individual CNT. (D) Corresponding HAADF-STEM image and elemental mapping for Pd_3Sn/CNT NHs.

of the hexagonal graphite (JCPDS-26-1080), which represents the CNTs component in the NHs, is also observed. Furthermore, the high-angle annular dark field-scanning TEM (HAADF-STEM) image and elemental mapping (Fig. 3D) demonstrate that the Pd and Sn elements are evenly distributed along the CNTs to form well-coupled NHs.

For comparison, other Pd_xSn_y/CNTs NHs with different compositions and crystal structures were synthesized using a similar preparation procedure as Pd_3Sn/CNTs. By only tuning the Pd and Sn metal precursors' molar ratios to 2 : 1, 3 : 2, and 1 : 1, the Pd_2Sn/CNTs, Pd_3Sn_2/CNTs, and PdSn/CNTs NHs can be obtained, respectively. As shown in Fig. S5–S7,† the microstructure and components characterized by TEM, XRD, and Raman spectra display that Pd_xSn_y NCs in the three samples were firmly bound to the outer wall of CNTs. The lattice fringes are spaced about 0.21, 0.28, and 0.33 nm, respectively, belongs to the (020) planes of orthorhombic phase Pd_2Sn (JCPDS-52-1515), the (002) planes of hexagonal phase Pd_3Sn_2 (JCPDS-4-801), and the (011) planes of orthorhombic phase PdSn (JCPDS-65-2603). The corresponding XRD patterns and Raman spectra further confirm the successful preparation of three Pd_xSn_y (Pd_2Sn, Pd_3Sn_2, and PdSn)/CNTs NHs.

3.2 Electrocatalytic evaluation of Pd_xSn_y/CNTs NHs

The ORR electrocatalytic performance of typical Pd_3Sn/CNTs NHs was tested by a standard three-electrode system with 0.1 M KOH solution as the electrolyte. Fig. 4A displays the cyclic voltammetry (CV) curves of Pd_3Sn/CNTs NHs in N_2- and O_2-saturated electrolytes, respectively. Compared with the N_2 atmosphere, a small cathode peak at around 0.83 V appeared under the O_2 atmosphere, indicating the potential ORR activity of Pd_3Sn/CNTs NHs. The ORR polarization curves (Fig. 4B) show that the current density of Pd_3Sn/CNTs NHs is gradually increased when the electrode rotation rates are raised from 400 to 2500 rpm, suggesting the ORR process on

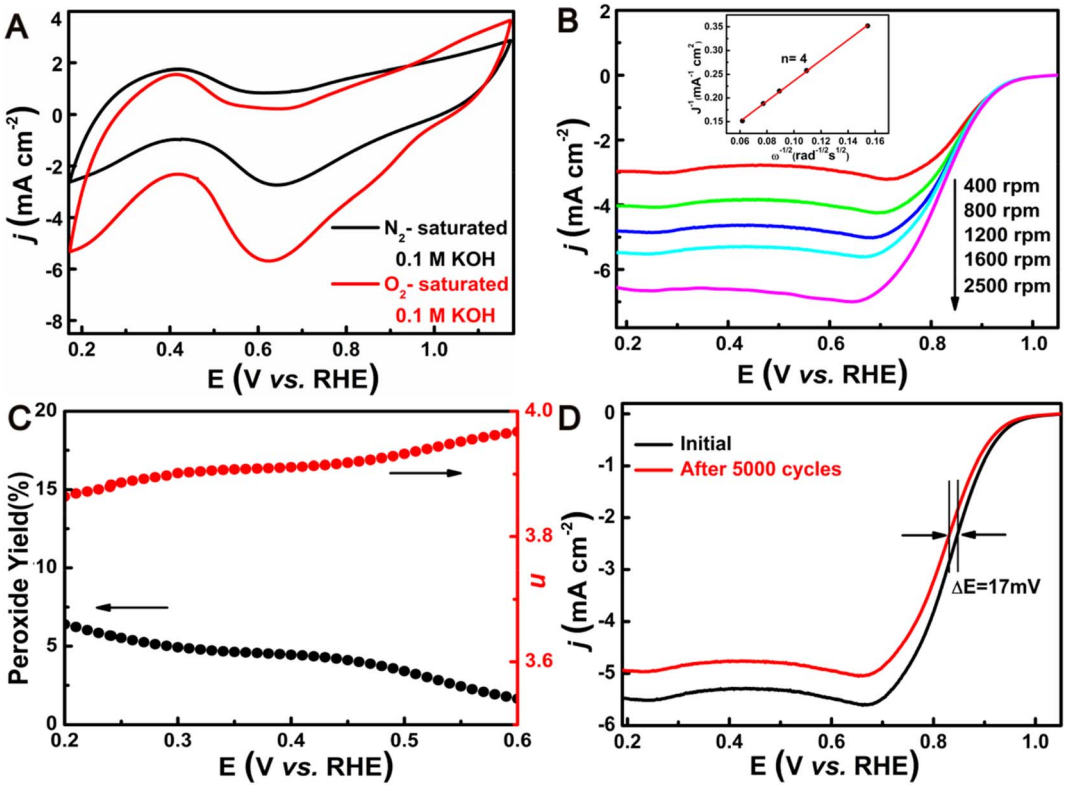

Fig. 4 (A) The CVs of Pd_3Sn/CNTs NHs. (B) ORR polarization plots of Pd_3Sn/CNTs NHs at different rotating rates. (C) The peroxide species yield (black color) and the number of transferred electrons (n) (red color) of Pd_3Sn/CNTs NHs. (D) The durability test for Pd_3Sn/CNTs NHs.

Pd_3Sn/CNTs NHs follows first-order kinetics. Meanwhile, the ORR polarization curve at 1600 rpm displayed that the Pd_3Sn/CNTs NHs exhibit an onset potential of 1.02 V (*vs.* RHE) and a half-wave potential of 0.85 V (*vs.* RHE), which are superior to many Pd-based alloys and multimetallic catalysts (Fig. S8A, B and Table S1†). Meanwhile, the pure Pd_3Sn NCs were synthesized as shown in Fig. S9A–D.† The onset potential and half-wave potential of Pd_3Sn/CNTs NHs are much more positive than that of pure CNT and pure Pd_3Sn NCs (Fig. S10†). In addition, the apparent current density of pure CNTs and pure Pd_3Sn NCs is lower than that of Pd_3Sn/CNTs NHs. Moreover, the Koutecky–Levich (K–L) plot calculated from the −0.6 V *vs.* Ag/AgCl shown in the inset of Fig. 4B implies the number of transferred electrons (n) during ORR is about 4.0, which is in accord with the result measured by RRDE (Fig. 4C), illustrating Pd_3Sn/CNTs NHs abides a "$4e^-$" pathway from O_2 to OH^-. In contrast to Pd_3Sn/CNTs NHs, the lower n values of pure CNT and pure Pd_3Sn NCs indicate that their reaction pathway is not exactly "$4e^-$" (Fig. S11A†). Meanwhile, the peroxide species yields (HO_2^-) on Pd_3Sn/CNTs NHs were lower than about 10% at different potentials (Fig. 4C), while that of pure CNT and pure Pd_3Sn NCs was significantly higher than that of Pd_3Sn/CNTs NHs (Fig. S11A†), highlighting the superior ORR efficiency of Pd_3Sn/CNTs NHs. In addition, electrochemical impedance spectroscopy shows that the presence of CNTs significantly reduced the interfacial charge transfer impedance of Pd_3Sn/CNTs NHs (Fig. S11B and C†). Also, Pd_3Sn/CNTs NHs displays superior catalytic stability compared to pure Pd_3Sn NCs (Fig. S11D†). Moreover, the durability tests measured by CV cycles (Fig. 4D) displayed that Pd_3Sn/CNTs NHs exhibited a slight negative shift in $E_{1/2}$ with a value of 17 mV after 5000 CV cycles, which is smaller than that of the commercial Pt/C catalyst (Fig. S12†), indicating that Pd_3Sn/CNTs NHs had good ORR stability. Furthermore, such Pd_3Sn/CNTs NHs have great methanol tolerance capability (Fig. S13†), showing application prospects on methanol fuel cells.

To highlight the superiority of Pd_3Sn/CNTs NHs on ORR activity, the Pd_2Sn/CNTs, Pd_3Sn_2/CNTs, and PdSn/CNTs catalysts were utilized for comparison. Impressively, Pd_3Sn/CNTs NHs show optimal E_{onset} and $E_{1/2}$ among all studied samples (Fig. 5A), which are more positive than those of Pd_2Sn/CNTs, Pd_3Sn_2/CNTs, and PdSn/CNTs. Additionally, Pd_3Sn/CNTs NHs present a more ideal "$4e^-$" ORR mechanism and lower HO_2^- yield in comparison with other samples (Fig. 5B). Moreover, the kinetic current density (J_k) of Pd_3Sn/CNTs NHs is computed to be 75.6 mA cm^{-2} at 0.55 V (*vs.* RHE), which is nearly 19.4, 3.3 and 2.3 times to PdSn/CNTs NHs, Pd_2Sn/CNTs NHs, and Pd_3Sn_2/CNTs NHs, respectively (Fig. 5C). Similarly, the mass activity (J_m) value of Pd_3Sn/CNTs NHs is superior to other samples yet (Fig. 5D and S14†). The above results confirmed that Pd_3Sn/CNTs NHs have the highest intrinsic activity.

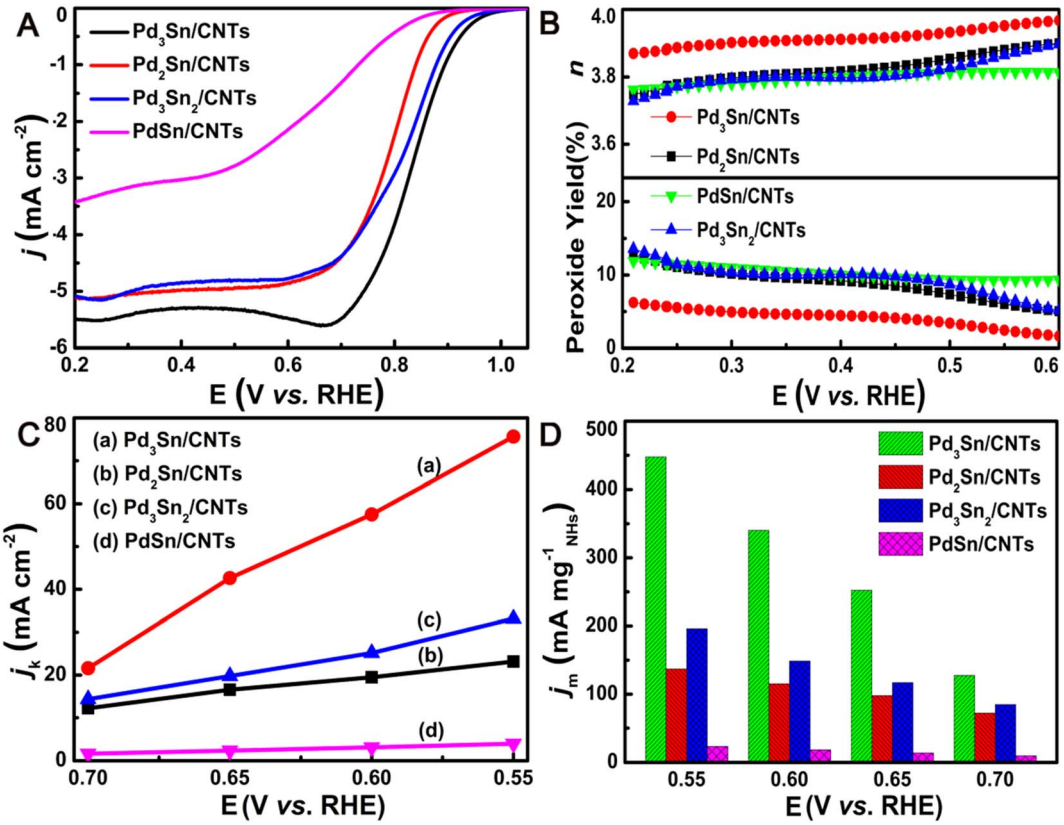

Fig. 5 (A) ORR polarization plots of the Pd_xSn_y/CNTs NHs at 1600 rpm. (B) The peroxide species yield and the number of transferred electrons (n) of Pd_xSn_y/CNTs NHs. (C) Kinetic current density (J_k) *versus* potential plots for those Pd_xSn_y/CNTs NHs. (D) Mass-specific activities of Pd_xSn_y/CNTs NHs.

4. Conclusions

In summary, a series of Pd_xSn_y (Pd_3Sn, Pd_2Sn, Pd_3Sn_2, PdSn)/CNTs NHs were successfully fabricated by *in situ* growth of Pd_xSn_y NCs on functionalized CNTs using a one-pot non-hydrolytic system thermolysis method. In those Pd_xSn_y/CNTs NHs, the Pd_xSn_y NCs were evenly distributed and anchored on the outer walls of CNTs, forming well-coupled NHs with high crystallinity. Such unique geometric structure can increase the electronic transport capability and catalytic durability, in favor of electrocatalytic applications. Electrochemical experiments proved that all Pd_xSn_y/CNTs NHs can well catalyze ORR. Among them, the Pd_3Sn/CNTs NHs display the best ORR catalytic capability with an onset potential and a half-wave potential of 1.02 and 0.85 V (*vs.* RHE), respectively. In addition, the stability and methanol tolerance capability of Pd_3Sn/CNTs NHs exceed Pt/C. According to TEM characterization and electrochemical test results, the great ORR activity of Pd_3Sn/CNTs NHs derives from their small size NCs building blocks, proper alloy component, and strong interplay or coupling between NCs and CNTs, which helps to increase mass activity and structure stability, even optimizes the adsorption/desorption on catalysts surface. This work is conducive to the advancement of Pd-based alloy catalysts or related NHs, and promoting their application in clean energy devices such as fuel cells and metal-air batteries.

Conflicts of interest

There are no conflicts to declare.

Acknowledgements

This work was financially supported by the National Natural Science Foundation of China (No. 21671106), the Priority Academic Program Development of Jiangsu Higher Education Institutions, the StartUp Fund for High-Leveled Talents from Fujian Normal University, and the Opening Research Foundation from the State Key Laboratory of Coordination Chemistry, Nanjing National Laboratory of Solid State Microstructures, Nanjing University.

References

1 Y. Yang, R. G. Agarwal, P. Hutchison, R. Rizo, A. V. Soudackov, X. Lu, E. Herrero, J. M. Feliu, S. Hammes-Schiffer, J. M. Mayer and H. D. Abruña, *Nat. Chem.*, 2022, **15**, 271–277.
2 V. R. Stamenkovic, D. Strmcnik, P. P. Lopes and N. M. Markovic, *Nat. Mater.*, 2016, **16**, 57–69.
3 S. Chu, Y. Cui and N. Liu, *Nat. Mater.*, 2016, **16**, 16–22.

4 M. Zhang, H. Li, J. Chen, F. X. Ma, L. Zhen, Z. Wen and C. Y. Xu, *Adv. Funct. Mater.*, 2022, **33**, 202209726.
5 J. Zhao, J. Lian, Z. Zhao, X. Wang and J. Zhang, *Nano-Micro Lett.*, 2022, **15**, 19.
6 F. Chang, Z. Bai, M. Li, M. Ren, T. Liu, L. Yang, C.-J. Zhong and J. Lu, *Nano Lett.*, 2020, **20**, 2416–2422.
7 H. Wang, W. Wang, H. Yu, Q. Mao, Y. Xu, X. Li, Z. Wang and L. Wang, *Appl. Catal., B*, 2022, **307**, 121172.
8 M. Zhao, H. Liu, H. Zhang, W. Chen, H. Sun, Z. Wang, B. Zhang, L. Song, Y. Yang, C. Ma, Y. Han and W. Huang, *Energy Environ. Sci.*, 2021, **14**, 6455–6463.
9 L. Li, B. Huang, X. Tang, Y. Hong, W. Zhai, T. Hu, K. Yuan and Y. Chen, *Adv. Funct. Mater.*, 2021, **31**, 202103857.
10 S. Zaman, L. Huang, A. I. Douka, H. Yang, B. You and B. Y. Xia, *Angew. Chem., Int. Ed.*, 2021, **60**, 17832–17852.
11 Z. Yu, S. Xu, Y. Feng, C. Yang, Q. Yao, Q. Shao, Y.-f. Li and X. Huang, *Nano Lett.*, 2021, **21**, 3805–3812.
12 C. Chen, Z. J. Tang, J. Y. Li, C. Y. Du, T. Ouyang, K. Xiao and Z. Q. Liu, *Adv. Funct. Mater.*, 2022, **33**, 202210143.
13 P. Cui, L. Zhao, Y. Long, L. Dai and C. Hu, *Angew. Chem., Int. Ed.*, 2023, **135**, e202218269.
14 B. Ji, J. Gou, Y. Zheng, X. Pu, Y. Wang, P. Kidkhunthod and Y. Tang, *Adv. Mater.*, 2023, **35**, 202300381.
15 G. Chen, Y. An, S. Liu, F. Sun, H. Qi, H. Wu, Y. He, P. Liu, R. Shi, J. Zhang, A. Kuc, U. Kaiser, T. Zhang, T. Heine, G. Wu and X. Feng, *Energy Environ. Sci.*, 2022, **15**, 2619–2628.
16 K. Huang, Y. Sun, Y. Zhang, X. Wang, W. Zhang and S. Feng, *Adv. Mater.*, 2018, **31**, 201801430.
17 Z. Wang, J. Huang, L. Wang, Y. Liu, W. Liu, S. Zhao and Z. Q. Liu, *Angew. Chem., Int. Ed.*, 2022, **134**, e202114696.
18 J. Zhang, J. Zhang, F. He, Y. Chen, J. Zhu, D. Wang, S. Mu and H. Y. Yang, *Nano-Micro Lett.*, 2021, **13**, 65.
19 T. Tang, W.-J. Jiang, X.-Z. Liu, J. Deng, S. Niu, B. Wang, S.-F. Jin, Q. Zhang, L. Gu, J.-S. Hu and L.-J. Wan, *J. Am. Chem. Soc.*, 2020, **142**, 7116–7127.
20 S. Zhao, J. Liu, C. Li, W. Ji, M. Yang, H. Huang, Y. Liu and Z. Kang, *ACS Appl. Mater. Interfaces*, 2014, **6**, 22297–22304.
21 H. Jin, H. Zhou, D. He, Z. Wang, Q. Wu, Q. Liang, S. Liu and S. Mu, *Appl. Catal., B*, 2019, **250**, 143–149.
22 Y. Yuan, Q. Zhang, L. Yang, L. Wang, W. Shi, P. Liu, R. Gao, L. Zheng, Z. Chen and Z. Bai, *Adv. Funct. Mater.*, 2022, **32**, 202206081.
23 Y. Wang, L. Tao, Z. Xiao, R. Chen, Z. Jiang and S. Wang, *Adv. Funct. Mater.*, 2018, **28**, 201705356.
24 C.-J. Li, G.-C. Shan, C.-X. Guo and R.-G. Ma, *Rare Met.*, 2023, **42**, 1778–1799.
25 T. Wang, A. Chutia, D. J. L. Brett, P. R. Shearing, G. He, G. Chai and I. P. Parkin, *Energy Environ. Sci.*, 2021, **14**, 2639–2669.
26 F. D. Sanij, P. Balakrishnan, P. Leung, A. Shah, H. Su and Q. Xu, *Int. J. Hydrogen Energy*, 2021, **46**, 14596–14627.
27 C. Huang, W. Dong, C. Dong, X. Wang, B. Jia and F. Huang, *Dalton Trans.*, 2020, **49**, 1398–1402.
28 X. Yuan, X. Wang, X. Liu, H. Ge, G. Yin, C. Dong and F. Huang, *ACS Appl. Mater. Interfaces*, 2016, **8**, 27654–27660.
29 M. Luo, Z. Zhao, Y. Zhang, Y. Sun, Y. Xing, F. Lv, Y. Yang, X. Zhang, S. Hwang, Y. Qin, J.-Y. Ma, F. Lin, D. Su, G. Lu and S. Guo, *Nature*, 2019, **574**, 81–85.
30 S. Liu, H. Ren, S. Yin, H. Zhang, Z. Wang, Y. Xu, X. Li, L. Wang and H. Wang, *Chem. Eng. J.*, 2022, **435**, 134823.
31 S. Liu, H. Zhang, T. Ren, H. Yu, K. Deng, Z. Wang, Y. Xu, L. Wang and H. Wang, *Small*, 2023, **19**, 202306014.
32 D. Liu, Y. Zhang, H. Liu, P. Rao, L. Xu, D. Chen, X. Tian and J. Yang, *Carbon Energy*, 2023, **5**, e327.
33 Y. Ge, X. Wang, B. Huang, Z. Huang, B. Chen, C. Ling, J. Liu, G. Liu, J. Zhang, G. Wang, Y. Chen, L. Li, L. Liao, L. Wang, Q. Yun, Z. Lai, S. Lu, Q. Luo, J. Wang, Z. Zheng and H. Zhang, *J. Am. Chem. Soc.*, 2021, **143**, 17292–17299.
34 S. Huang, S. Lu, H. Hu, F. Xu, H. Li, F. Duan, H. Zhu, H. Gu and M. Du, *Chem. Eng. J.*, 2021, **420**, 130503.
35 Z. Liu, X. Yang, L. Cui, Z. Shi, B. Lu, X. Guo, J. Zhang, L. Xu, Y. Tang and Y. Xiang, *Part. Part. Syst. Charact.*, 2018, **35**, 1700366.
36 D. Wang, H. L. Xin, H. Wang, Y. Yu, E. Rus, D. A. Muller, F. J. DiSalvo and H. D. Abruña, *Chem. Mater.*, 2012, **24**, 2274–2281.
37 D. Wang, H. L. Xin, R. Hovden, H. Wang, Y. Yu, D. A. Muller, F. J. DiSalvo and H. D. Abruna, *Nat. Mater.*, 2013, **12**, 81–87.
38 W. Xiao, M. A. L. Cordeiro, G. Gao, A. Zheng, J. Wang, W. Lei, M. Gong, R. Lin, E. Stavitski, H. L. Xin and D. Wang, *Nano Energy*, 2018, **50**, 70–78.
39 X. Lu, M. Ahmadi, F. J. DiSalvo and H. D. Abruña, *ACS Catal.*, 2020, **10**, 5891–5898.
40 Y. Wu, C. Wang, L. Zou, Q. Huang and H. Yang, *J. Electroanal. Chem.*, 2017, **789**, 167–173.
41 Y. Ocak, S. Aksöz, N. Maraşlı and E. Çadırlı, *Fluid Phase Equilib.*, 2010, **295**, 60–67.
42 S. Bose, V. Bhattacharya, K. Chattopadhyay and P. Ayyub, *Acta Mater.*, 2008, **56**, 4522–4528.
43 M. Lüsi, H. Erikson, H.-M. Piirsoo, P. Paiste, J. Aruväli, A. Kikas, V. Kisand, A. Tamm and K. Tammeveski, *J. Electroanal. Chem.*, 2022, **917**, 116391.
44 J. Liang, S. Li, Y. Chen, X. Liu, T. Wang, J. Han, S. Jiao, R. Cao and Q. Li, *J. Mater. Chem. A*, 2020, **8**, 15665–15669.
45 Y. Zhang, B. Huang, Q. Shao, Y. Feng, L. Xiong, Y. Peng and X. Huang, *Nano Lett.*, 2019, **19**, 6894–6903.
46 H. Erikson, A. Sarapuu, J. Solla-Gullón and K. Tammeveski, *J. Electroanal. Chem.*, 2016, **780**, 327–336.
47 P. Pachfule, D. Shinde, M. Majumder and Q. Xu, *Nat. Chem.*, 2016, **8**, 718–724.
48 G. Zhou, D. W. Wang, L. C. Yin, N. Li, F. Li and H. M. Cheng, *ACS Nano*, 2012, **6**, 3214–3223.
49 E. McCalla, A. M. Abakumov, M. Saubanère, D. Foix, E. J. Berg, G. Rousse, M.-L. Doublet, D. Gonbeau, P. Novák, G. V. Tendeloo, R. Dominko and J. M. Tarascon, *Science*, 2015, **350**, 1516–1521.
50 Y. S. Kang, K.-H. Choi, D. Ahn, M. J. Lee, J. Baik, D. Y. Chung, M.-J. Kim, S. Y. Lee, M. Kim, H. Shin, K.-S. Lee and Y.-E. Sung, *J. Power Sources*, 2016, **303**, 234–242.